

Optical wavelength converters for photonic band gap microcircuits

Dragan Vujic* and Sajeev John

Department of Physics, University of Toronto, 60 St. George Street, Toronto, Ontario, Canada M5S-1A7

(Received 8 January 2009; published 18 May 2009)

We demonstrate compact optical wavelength conversion architecture for picosecond laser pulses and data streams within photonic band gap waveguides. These multimode waveguides are seeded with resonantly driven, inhomogeneously broadened, distributions of quantum dots whose optical transition center frequency is placed near a sharp discontinuity in the local (electromagnetic) density of states (LDOS). This discontinuity is provided by a cutoff in one of the waveguide modes. Wavelength conversion of an optical pulse propagating in the single-mode spectral range of the waveguide, near the LDOS jump, is provided by a steady-state holding field with frequency matched to the center frequency of the quantum dot distribution. In the absence of an incident laser pulse, the holding field is absorbed by the quantum dots. When the incident pulse intensity is sufficient to cause population inversion of a suitable fraction of the quantum dots, the holding field is amplified and the incident pulse profile is imprinted on to the holding field, leading to wavelength conversion in the range of 3–20 nm at wavelengths near 1.5 μm . Larger wavelength shifts typically require higher power levels for operation (milliwatt scale) but enable conversion of shorter (picosecond) pulses. Small wavelength shifts typically require narrower distribution of quantum dot resonance frequencies. Using finite-difference time-domain simulations, we show that an optical pulse (Gaussian in time) can create another equivalent optical pulse with either higher or lower center frequency inside the photonic band gap of the structure. Optical pulses of a given center frequency can also be selectively amplified or absorbed depending on the coincident arrival of another laser pulse with different center frequency, enabling all-optical logic operations within a multiwavelength-channel optical circuit.

DOI: [10.1103/PhysRevA.79.053836](https://doi.org/10.1103/PhysRevA.79.053836)

PACS number(s): 42.79.Nv, 42.65.Pc, 42.50.Gy, 42.79.Ta

I. INTRODUCTION

Photonic band gap (PBG) materials [1,2] are artificial periodically microstructured dielectrics that facilitate the trapping and localization of light [3]. Nonlinear photonic crystal (PC) waveguides are attractive owing to their fast optical response and low optical power requirements. They offer an opportunity to create compact all-optical switches that can be integrated into an optical microchip [4–10] and provide a novel basis for all-optical information processing. In contrast to present day's electronic computing operating with only a single channel of information in a current path, the PBG waveguide can conduct many different wavelength channels of information simultaneously. All-optical circuits and integrated logic devices may require the interconversion of data streams between different frequency channels. All-optical wavelength conversion in nonlinear photonic crystals is a subject of intensive investigation today [11–15]. In this paper, we describe a method for wavelength conversion inside photonic crystal waveguides seeded with resonant quantum dots. Our numerical simulations show that one short laser pulse (with temporal duration on the order of a picosecond) can induce a new optical pulse of the same shape but with different central frequency through coherent optical interaction with the quantum dots. With appropriately chosen waveguide architecture and quantum dot transition frequencies, this device can either raise or lower the central wavelength of a picosecond scale pulse, without pulse distortion, by up to 20 nm for pulses centered near 1.5 μm .

We also identify fundamental trade-offs involving the stochasticity in position and sizes of quantum dots (inhomogeneous broadening), the extent of the wavelength shift achieved, and the power levels required for wavelength conversion. In general small amount of inhomogeneous broadening ($\sim 1\%$) is advantageous and provides bandwidth in the gain spectrum for converting ultrashort (picosecond) pulses.

Such a distribution of quantum dots leads to about 20 nm wavelength shift between input and output pulses using milliwatt power optical holding field. When the inhomogeneous broadening is larger than 1% shorter pulses can be converted, but higher power levels are required and minimum possible wavelength shift is increased.

II. WAVEGUIDE ARCHITECTURES FOR WAVELENGTH CONVERSION

In order to demonstrate frequency conversion in photonic crystal waveguides, we choose an idealized two-dimensional (2D) structure consisting of a square lattice (lattice constant a) of dielectric rods made of GaAs ($\epsilon_r=9$) with radius $r=0.3a$, embedded in air. This structure has a band gap for the transverse magnetic (TM) -polarized light between $\omega_{\min}=0.265(2\pi c/a)$ and $\omega_{\max}=0.335(2\pi c/a)$, where c is speed of light in vacuum. In order to achieve Q -dot switching through resonance fluorescence in photonic band gap waveguides we introduce specific waveguide architectures that provide large jump discontinuities in the local electromagnetic density of states inside the PBG. We present four examples of multimode waveguide architectures (shown in Figs. 1–8) suitable for optical switching using resonance fluorescence. They consist of 2D dielectric square lattices

*dvujic@physics.utoronto.ca

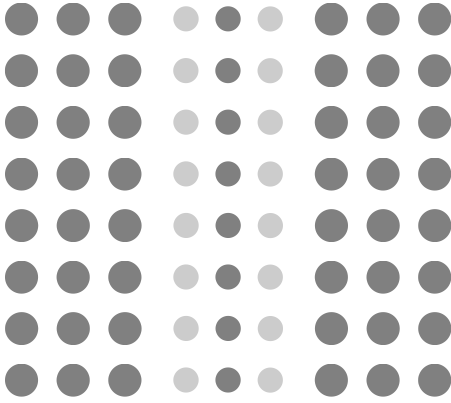


FIG. 1. Architecture 1. The crystal consists of a square-lattice layer of dielectric rods ($\epsilon=9$) with radius $r=0.3a$ in air (embedded within a 3D heterostructure). Multimode waveguide is made by reducing the radius of three lines of dielectric rods to $0.225a$ and moving outer defect lines toward the central one by $\frac{5.5a}{30}$.

containing multimode waveguides. In a real three-dimensional (3D) system, the idealized 2D PC is replaced with a thin 2D PC layer, sandwiched by 3D PBG material above and below [16]. This prevents light propagation in the vertical direction perpendicular to the 2D plane and also provides a large jump in the 3D electromagnetic density of states [8].

Architecture 1 (Fig. 1) consists of changing the radius of the dielectric rods in three adjacent lines from $r=0.3a$ to $r=0.225a$. The two outer lines of reduced dielectric rods are shifted toward the middle by $5.5a/30$ in order to increase the group velocity of the signal. This architecture provides a large jump in the local density of states (LDOS) at the position of reduced dielectric rods in two outer defect lines (gray circles in Fig. 1) where the quantum dots are located. Quan-

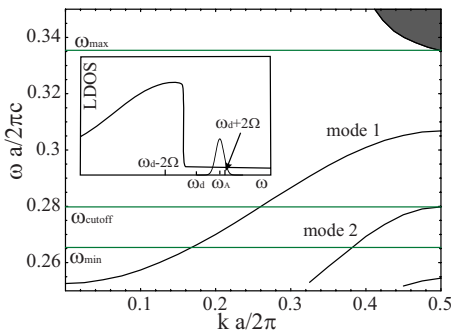


FIG. 2. (Color online) Dispersion lines of the waveguide shown in Fig. 1, calculated at resolution of 30 points per lattice constant, using FDTD method. (a) Propagation mode (mode 1) allows the system to receive and transmit ultrafast pulses ($v_g \approx 0.16c$) and (b) cutoff mode (mode 2) provides a large jump of the local density of states around cutoff frequency [$\omega_{\text{cutoff}}=0.2798(2\pi c/a)$]. A schematic representation of the LDOS generated inside the waveguide and the relevant frequencies for resonance fluorescence are shown in the inset. $\omega_d - 2\Omega$ and $\omega_d + 2\Omega$ are the Mollow fluorescence sidebands generated by strong laser field of frequency ω_d , Ω is the Rabi frequency, and atomic transition frequencies are distributed around central atomic transition frequency ω_A .

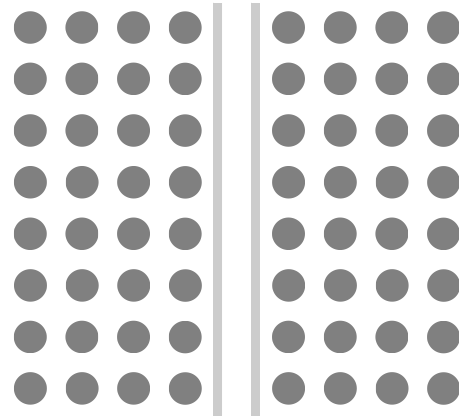


FIG. 3. Architecture 2 consists of a 2D layer (embedded within a 3D heterostructure), exhibiting a discontinuous electromagnetic density of states. The waveguide is made by exchanging one line of dielectric rods with two dielectric strips. Thickness of each strip is $0.17a$ and they are separated from each other either by an air gap of $0.59a$.

tum dot resonance frequencies are normally distributed around the central atomic transition frequency [$\omega_A = 0.285(2\pi c/a)$] with full width at half maximum (FWHM) of 0.5%. Above the cutoff frequency of mode 2 [$\omega_{\text{cutoff}} = 0.2798(2\pi c/a)$], we have a single-mode waveguide suitable for signal pulse propagation (see Fig. 2). The group velocity of the single mode 1 near the cutoff frequency is $0.16c$. Architecture 1 enables the generation of a signal pulse with higher central frequency than the driving field center frequency. Accordingly, we refer to architecture 1 as a frequency up-conversion switch.

The waveguide of architecture 2 (see Fig. 3) is made by exchanging one line of dielectric rods with two thin dielectric strips. The thickness of each dielectric strip is $0.17a$ and they are separated from each other by $0.59a$. This architecture provides the dispersion curves shown in Fig. 4. We use this architecture to generate a signal pulse with lower center frequency than the driving field center frequency. Accord-

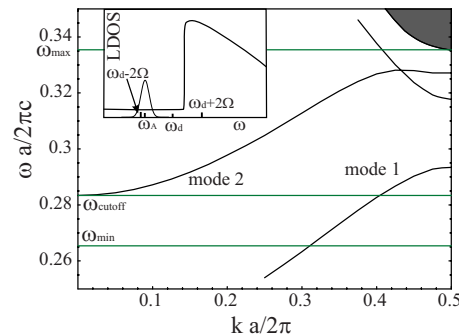


FIG. 4. (Color online) Dispersion curves of the waveguide shown in Fig. 3. Mode 2 provides a large jump in the local density of states around cutoff frequency [$\omega_{\text{cutoff}}=0.2834(2\pi c/a)$], while mode 1 allows fast light propagation (with group velocity of $v_g \approx 0.2c$) in the single-mode frequency domain below cutoff frequency. The inset depicts the LDOS generated inside the waveguide in the vicinity of cutoff frequency relevant to resonance fluorescence.

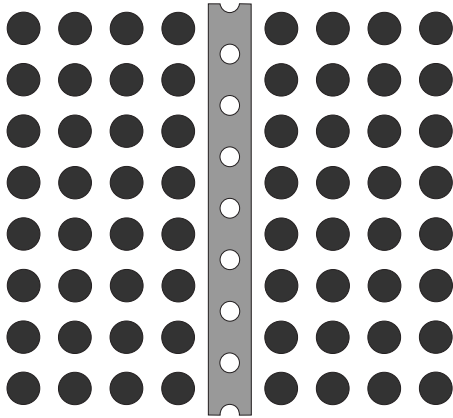


FIG. 5. Architecture 3. This wavelength converter consists of a 2D layer (embedded within a 3D heterostructure), made of dielectric rods ($n=3$) with radius $0.3a$. A multimode waveguide is made by omitting one line of dielectric rods, and including a $0.425a$ thick dielectric strip containing air hole with radius $r=0.175a$. Air holes are centered in the middle between two dielectric rods of original structure.

ingly, we will refer to architecture 2 as a frequency down-conversion switch. In the single-mode frequency region of mode 1 between ω_{\min} and ω_{cutoff} (see Fig. 4), the group velocity is $v_g \approx 0.2c$. This allows fast signal pulse propagation. Mode 2, with cutoff frequency $\omega_{\text{cutoff}}=0.2834(2\pi c/a)$, provides a large jump in the local density of state needed for quantum dot switching through resonance fluorescence [10]. Dielectric strips are seeded with quantum dots with resonance frequencies normally distributed with FWHM of 0.5%. The gray color of the dielectric strips in Fig. 3 is chosen to highlight the location of the quantum dots.

In architecture 3, the waveguide consists of exchanging dielectric rods along one line of the 2D PC layer with a

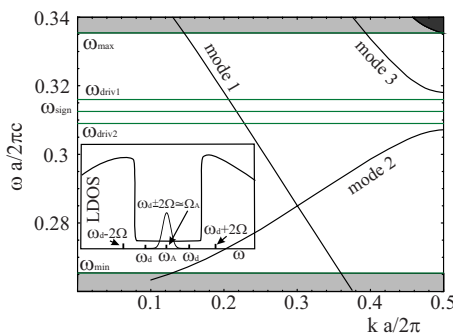


FIG. 6. (Color online) Dispersion lines for architecture 3 shown in Fig. 5, calculated at resolution of 30 pixels per lattice constant, using FDTD method. (a) Propagating mode (mode 1) facilitates ultrafast signal pulse propagation ($v_g \approx 0.32c$) and (b) cutoff modes (mode 2 and mode 3) provide large jumps of the local density of states around cutoff frequencies. A schematic representation of the LDOS generated inside the waveguide and the relevant frequencies for resonance fluorescence are shown in the inset. High intensity driving field can be located in either of the two marked positions ω_d (see inset). We maintain driving field power such that one Mollow sideband coincides with the atomic line center transition frequency, while other Mollow sideband is located in one of the high LDOS regions.

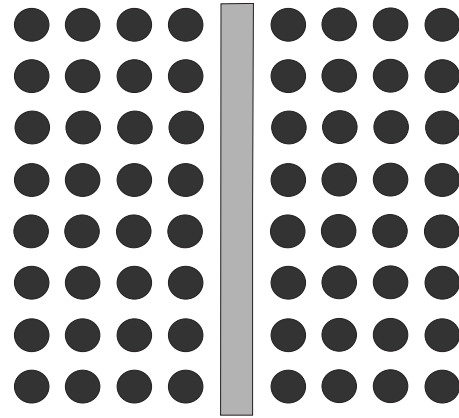


FIG. 7. Architecture 4. A bimodal PC waveguide is made by omitting one line of dielectric rods and including an $0.3a$ thick dielectric strip inside a thin 2D PC square lattice sandwiched by 3D PBG material.

periodically patterned dielectric strip (see Fig. 5). The thickness of the strip is $0.425a$ and it is patterned with air cylinders of radius $r=0.175a$ (see Fig. 5). These air cylinders are displaced along the waveguide axis by $a/2$ relative to the dielectric rods of the background PC layer. The dielectric strip is seeded with quantum dots with resonance frequencies normally distributed around $\omega_A=0.3125(2\pi c/a)$ with FWHM of 0.7%. Dispersion lines of this multimode waveguide, calculated by finite-difference time-domain (FDTD) method with resolution of 30 points per lattice constant, are shown in Fig. 6. The propagation mode 1 has high group velocity of $v_g \approx 0.32c$, enabling ultrafast signal pulse propagation. The other two modes have cutoff frequencies at $0.3072(2\pi c/a)$ (mode 2) and $0.3180(2\pi c/a)$ (mode 3). Cutoff frequencies of these two modes bound the narrow single-mode frequency domain of the waveguide from above and below. Large jumps of the electromagnetic LDOS occur at both bounding frequencies as shown in the inset of Fig. 6. Architecture 3 has LDOS jumps on both sides of the quantum dot transition frequencies and can be used for either up-conversion or down-conversion switching.

Architecture 4 is small variation of architecture 3 where we simply omit the small air cylinders from the dielectric

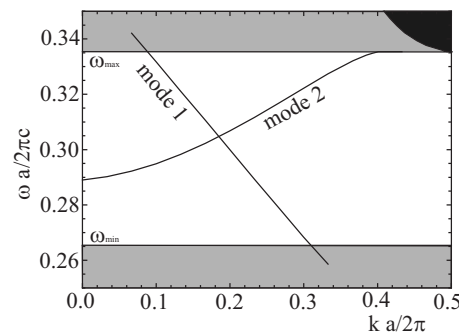


FIG. 8. Dispersion curves of the bimodal waveguide shown in Fig. 7, calculated at resolution of 20 points per lattice constant using FDTD method. Mode 1 (propagating mode) has a group velocity of ($v_g \approx 0.31c$), while mode 2 has cutoff at $\omega_{\text{cutoff}}=0.289(2\pi c/a)$, providing a large jump of the local density of states.

strip in order to simplify fabrication. We also reduce the thickness of the solid strip to $0.3a$. This architecture provides large jump of the local electromagnetic density of states at the cutoff frequency of mode 2 [$\omega_{\text{cutoff}}=0.289(2\pi c/a)$]. Ultrafast light pulse propagation is considered in mode 1 (propagating mode) at frequencies below ω_{cutoff} . We use this architecture to demonstrate wavelength conversion with smaller wavelength shift of around 3 nm. To achieve such a small frequency shift, we must seed the dielectric strip with nearly identical quantum dots with very narrowly distributed resonances (FWHM=0.05%) around the central transition frequency [$\omega_A=0.28795(2\pi c/a)$].

III. QUANTUM DOT RESPONSE TO DRIVING AND SIGNAL FIELDS

The quasi-steady-state response of the quantum dots inside a PC waveguide has been discussed in detail elsewhere [9,10]. We recapitulate only the main results here. A collection of two-level atomic systems in the vicinity of the large jump of the LDOS, driven by a strong enough laser field, can be described by a real time-dependent susceptibility

$$\chi^{(1)}(x,y,t) = A e^{-\Gamma_{\text{coh}} t} [-\gamma_+ \mathbf{c}^4 (\pi_2 - \pi_1) \sin(\omega_L + 2\Omega)t - \gamma_- \mathbf{s}^4 (\pi_1 - \pi_2) \sin(\omega_L - 2\Omega)t]. \quad (1)$$

Here, $A \approx \frac{|\mu|^2 T_2 N}{\epsilon_0 \hbar}$, where N is average number of quantum dots per unit volume, ϵ_0 is the permittivity of free space, \hbar is the Planck constant, μ is average dipole transition matrix element of the Q dots, and $T_2=1/\gamma_p$ is dephasing time arising from phonon interactions. Equation (1) describes the nonlinear response of the Q dots to a cw laser field with Rabi frequency Ω (as defined below). However, Eq. (1) only describes the linear response to an additional weak signal pulse (the optical pulse that we wish to up convert or down convert in frequency). Strictly speaking, Eq. (1) describes the steady-state susceptibility of the Q dots. In what follows, we extrapolate this response to moderately short (picosecond) pulses. A more precise description of both nonlinearity and the dynamics requires evaluation of the dynamical response of the Q -dot Bloch vector. This more precise formulation in fact reveals [17] an even more dramatic and robust switching effect that is not apparent in the present quasi-steady-state linearized response.

For illustration purposes, we chose realistic values $\mu = 1.09 \times 10^{-28}$ C m [18,19] and $T_2=2$ ns [20–24], corresponding to InGaAs/GaAs and InAs/InGaAs quantum dots at very low temperatures. The generalized Rabi frequency, $\Omega(x,y,t) = [(\frac{\mu A^d(x,y,t)}{\hbar})^2 + \frac{\Delta_{Ad}^2(x,y)}{4}]^{1/2}$ is spatially dependent according to the light intensity distribution and the different transition frequencies of the Q dots located in different positions inside the waveguide. Here, $\Delta_{Ad} = \omega_A(x,y) - \omega_d$ is the detuning between atomic transition frequency and driving field frequency and $A^d(x,y,t) = \sqrt{2 \langle [\mathbf{E}^d(x,y,t)]^2 \rangle}$ is the amplitude of the driving field at the position (x,y) . The angular brackets denote a time averaging. Γ_{coh} is the decay rate for the atomic coherence [9,10] and γ_0 , γ_- , and γ_+ are radiative decay rates at the spectral positions of driving field and Mollow sidebands. We choose realistic values (10^9 s $^{-1}$) for de-

cay rates in the single-mode frequency domain and 500 times more rapid decay in the high LDOS frequency region [8,10]. π_2 and π_1 are the equilibrium excited and ground dressed state populations ($\pi_2 = \frac{\gamma_- \mathbf{s}^4}{\gamma_- \mathbf{s}^4 + \gamma_+ \mathbf{c}^4}$ and $\pi_1 = \frac{\gamma_+ \mathbf{c}^4}{\gamma_- \mathbf{s}^4 + \gamma_+ \mathbf{c}^4}$), while parameters \mathbf{c} and \mathbf{s} are defined as follows: $\mathbf{s}^2 = \frac{1}{2} [1 - \frac{\Delta_{Ad}}{\Omega}]$, $\mathbf{c}^2 = \frac{1}{2} [1 + \frac{\Delta_{Ad}}{\Omega}]$. A detailed derivation of this model can be found in previous literature [9,25]

In order to investigate light propagation through our PC waveguides we solve the coupled equations for optical signal propagation and quantum dot response. By employing a piecewise linear recursive convolution approach [26,27] we solve Maxwell's equations [Eq. (2a)–(2d)] in the 2D PC waveguide, for the TM-polarized light. Since the optical pulse and cw laser fields are well separated in frequency, we use two sets of Maxwell's equations with superscripts s for signal field and d for driving field in order to determine propagation characteristics of both beams,

$$\frac{\partial D_z^{s,d}}{\partial t} = \left(\frac{\partial H_y^{s,d}}{\partial x} - \frac{\partial H_x^{s,d}}{\partial y} \right), \quad (2a)$$

$$\mu_0 \frac{\partial H_x^{s,d}}{\partial t} = - \frac{\partial E_z^{s,d}}{\partial y}, \quad (2b)$$

$$\mu_0 \frac{\partial H_y^{s,d}}{\partial t} = \frac{\partial E_z^{s,d}}{\partial x}, \quad (2c)$$

$$D_z^{s,d}(x,y,t) = \epsilon_0 \epsilon_r(x,y) E_z^{s,d}(x,y,t) + \epsilon_0 \int_0^t E_z^{s,d}(x,y,t-\tau) \chi^{(1)}(x,y,\tau) d\tau. \quad (2d)$$

Here, $\chi^{(1)}(x,y,\tau)$ is the total susceptibility of the ensemble of Q dots given by Eq. (1), within the dielectric material seeded with quantum dots and zero outside nonlinear area, μ_0 is the permeability of free space, and $\epsilon_r(x,y)$ is the dielectric constant of the undoped photonic crystal rods (for GaAs $\epsilon_r=9.0$).

In order to estimate overall power levels in a PC waveguide in a realistic 3D architecture we assume uniform light distribution in the third dimension (orthogonal on light propagation) inside 0.3a thick 2D PC layer and zero light intensity above and below.

IV. NUMERICAL SIMULATION OF TRANSMISSION SPECTRA

As a first set of numerical experiments, we calculate steady-state transmission power spectrum,

$$T(\omega) = P_{\text{out}}(\omega)/P_{\text{in}}(\omega), \quad (3)$$

using a continuous wave as the driving field for all architectures. To this end, we place our source at the middle of the input port of the PC waveguide. In our numerical simulations an absorber is placed all around the computational domain in order to prohibit unwanted reflections. We measure frequency dependent power by placing two line detectors across

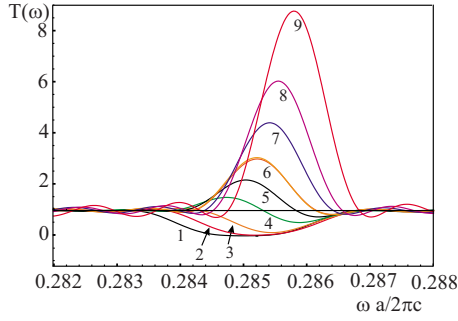


FIG. 9. (Color online) Steady-state power transmission spectrum of the 20 unit cell long active part of the waveguide shown in Fig. 1. The gray area in Fig. 1 is seeded with $N=6.7 \times 10^4$ dots/ $(\mu\text{m})^3$ centered around $\omega_A=0.285(2\pi c/a)$ with FWHM of 0.5%. Device is controlled with continuous wave driving powers of (1) 0.0, (2) 0.3, (3) 0.54, (4) 0.84, (5) 1.02, (6) 1.18, (7) 1.42, (8) 1.65, and (9) 2.15 mW, oscillating at $\omega_d=0.2815(2\pi c/a)$. Power is estimated for a realistic $0.3a$ thick 2D PC layer sandwiched by 3D PBG structure.

the waveguide in front of and behind the nonlinear part of the waveguide. The input power spectrum is denoted by $P_{\text{in}}(\omega)$, while $P_{\text{out}}(\omega)$ denotes output power spectrum. In the low driving field power regime, the quantum dots provide absorption over the bandwidth of the quantum dot distribution (curve 1 in Fig. 9). By increasing the cw power, more and more quantum dots undergo the transition from an absorbing to an amplifying state as evidenced by subsequent transmission spectra presented in Fig. 9. Higher powers provide higher amplification, but very high powers also change the dispersive properties of the waveguide.

In Fig. 10, we present the steady-state power transmission spectrum for optical waves propagating through (a 20 unit cell long active region) architecture 2 (left panel) and archi-

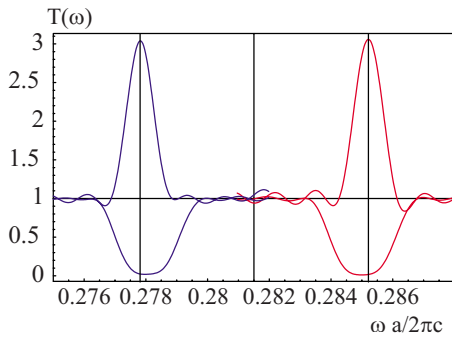


FIG. 10. (Color online) Steady-state power transmission spectrum of the 20 unit cell long active part of the frequency down-conversion switch (left) shown in Fig. 3 and frequency up-conversion switch (right) shown in Fig. 1. Both devices are controlled with continuous wave driving powers of 1.18 mW (amplification) and 0.0 mW (absorption), oscillating at $\omega_d=0.2815(2\pi c/a)$. Power is rescaled for the more realistic $0.3a$ thick 2D layer covered with 3D structure. Atomic transition frequencies are centered around $\omega_A=0.27805(2\pi c/a)$ in architecture 2 and around $\omega_A=0.285(2\pi c/a)$ in architecture 1, with FWHM of 0.5%. Concentration of quantum dots is $N=6.7 \times 10^4$ dots/ $(\mu\text{m})^3$ in the both architectures.

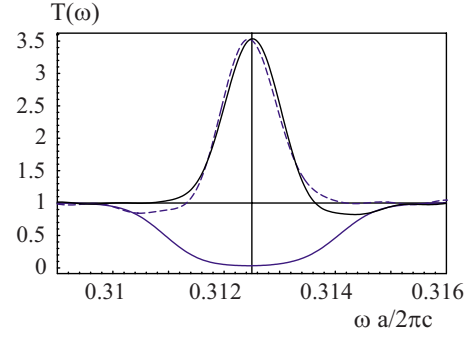


FIG. 11. (Color online) Steady-state power transmission spectrum of the 20 unit cell long active part of the waveguide shown in Fig. 5 seeded with $N=6.0 \times 10^4$ dots/ $(\mu\text{m})^3$ inside dielectric strip. The device is controlled with continuous wave driving powers of 2.36 mW (amplification) and 0.0 mW (absorption). Power is rescaled for the $0.3a$ thick 2D layer covered with 3D structure. Atomic transition frequencies are centered around $\omega_A=0.3125(2\pi c/a)$ with FWHM of 0.7%. We provided two sets of numerical simulations with two different values of driving field frequencies: $\omega_d=0.309(2\pi c/a)$ (solid line) and $\omega_d=0.316(2\pi c/a)$ (dashed line).

ture 1 (right panel). Both waveguides are seeded with the same type of quantum dots (parameters chosen for InGaAs/GaAs or InAs/InGaAs quantum dots) normally distributed (with FWHM of 0.5%) around central atomic transition frequencies $\omega_A=0.285(2\pi c/a)$ in architecture 1 and $\omega_A=0.27805(2\pi c/a)$ in architecture 2. In order to obtain peak amplification by a factor of 3 in both devices, we seeded them with $N=6.7 \times 10^4$ dots/ $(\mu\text{m})^3$ inside outer two lines of reduced dielectric rods in architecture 1 (see gray area in Fig. 1) and inside dielectric strips of architecture 2 (see gray area in Fig. 3). The average dot center to dot center distance in this case is around 30 nm in horizontal direction and around 17 nm in vertical dimension. It is important to note that the both devices are controlled with the same continuous wave driving powers of 1.18 mW in the amplifying regime and 0.0 mW in absorbing regime, oscillating at $\omega_d=0.2815(2\pi c/a)$. This power provides large amplification of the signal field (see Fig. 10) centered at $0.27785(2\pi c/a)$ in architecture 2 and centered at $0.2852(2\pi c/a)$ in architecture 1. Our power estimate is based on a more realistic $0.3a$ thick 2D PC layer sandwiched by a 3D PBG structure [8,10,16].

The transmission spectrum of (20 unit cell long nonlinear part) architecture 3 waveguide is shown in Fig. 11. We use the same quantum dot parameters as in previous two architectures, but this time with resonance frequency distribution of 0.7%, around central transition frequency $\omega_A=0.3125(2\pi c/a)$. Quantum dots are located inside the dielectric strip (see gray area in Fig. 5) with concentration of $N=6.0 \times 10^4$ dots/ $(\mu\text{m})^3$. In the low driving intensity regime, all quantum dots are absorbing and the transmission spectrum mirrors the quantum dot distribution profile (lower curve in Fig. 11). In the amplifying regime we consider two separate variations in the switching device. In both variations, amplification regime is established using cw driving power of 2.36 mW (estimated for a $0.3a$ thick 2D PC layer sandwiched by 3D PBG materials). In the first variation, the driving field frequency is $\omega_d=0.309(2\pi c/a)$ and the trans-

mission spectrum is given by the upper solid line in Fig. 11. In the second variation (dashed line in Fig. 11) the driving field oscillates at $\omega_d=0.316(2\pi c/a)$. Both transmission spectra are centered around the same frequency [Q -dot line center $\omega_A=0.3125(2\pi c/a)$]. This allows amplification of the same signal beam oscillating at $\omega_s=\omega_A=0.3125(2\pi c/a)$, with driving fields on either side of the signal pulse center frequency.

V. NUMERICAL SIMULATION OF PULSE WAVELENGTH CONVERSION

We now consider frequency conversion in (20 unit cell long active region) the PC waveguides of Figs. 1, 3, and 5. We launch a high intensity laser pulse (Gaussian in time with temporal duration of 2 ps) [28], in the presence of another low intensity cw optical field, at the input port of each waveguide. We measured time-dependent power profiles of both fields at input and output ports of the waveguides. The power of the high intensity laser pulse (driving field) is assumed uniform in the out-of-plane direction over a $0.3a$ thick 2D layer in order to simulate the behavior of a device embedded in a 2D-3D PBG heterostructure [8,29]. The low intensity signal field is given in arbitrary units. Our numerical studies demonstrate that a high intensity laser pulse entering the waveguide can create new optical pulse in the output port of the waveguide with new central frequency determined by the cw field. Frequencies of the incoming high intensity pulse (driving field) and the output frequency-converted optical pulse depend on the waveguide architecture, detuning between quantum dots and driving pulse, and distribution of quantum dots in the spatial and frequency domains. This flexibility may prove attractive for applications in optical communications and optical computing. We now present detailed numerical results for our frequency conversion devices.

In architecture 2 (see Fig. 3), we seed quantum dots in the single-mode domain below the cutoff frequency of mode 2 (see Fig. 4), with inhomogeneously broadened line center $\omega_A=0.27805(2\pi c/a)$. Slightly below the transition center frequency of quantum dots, we place one low intensity cw laser beam oscillating at the frequency $\omega_s=0.27785(2\pi c/a)$, where the transmission of the device is maximum (see Fig. 10). The cw beam oscillates at a frequency within the bandwidth of the quantum dot distribution. Therefore, in the absence of the driving pulse, the cw field is absorbed and completely attenuated when it reaches the output port of the waveguide [see Fig. 10 (left) and Fig. 12]. We switch the system with one high intensity laser pulse, oscillating at frequency $\omega_d=0.2815(2\pi c/a)$ in the single-mode region of the multimode waveguide, located between the cutoff frequency and atomic central transition frequency. This provides a contrast in the LDOS experienced by the two Mollow sidebands produced by the driving pulse. As the power of the driving field increases and decreases gradually, individual atomic dipoles undergo switching from absorbing to amplifying and back to absorbing behavior. This imprints the driving field profile onto the output signal field (see Fig. 12) with lower central frequency. This device acts as a down-conversion switch.

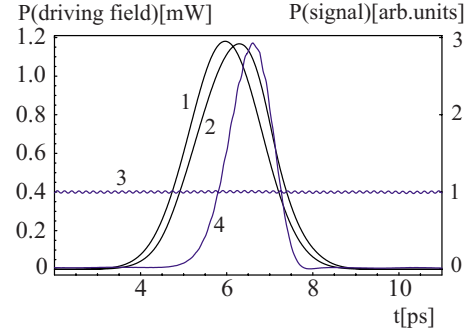


FIG. 12. (Color online) Incident and transmitted time-dependent powers of the high intensity laser pulse (driving field), Gaussian in time, with temporal duration of 2 ps and central frequency of $0.2815(2\pi c/a)$ (curves 1 and 2, respectively), and low intensity signal field (curve 3) propagating through architecture 2 (Fig. 3). The signal field has the form of cw beam oscillating at $0.27785(2\pi c/a)$ in the input port of the down-conversion switch and appears as a pulse (curve 4) in the output port of the waveguide. Essentially the same picture is observed if the signal field is replaced by a cw beam oscillating at $0.2852(2\pi c/a)$ at the input port in the up-conversion switch of architecture 1 (Fig. 1).

In contrast to architecture 2, architecture 1 has single-mode frequency domain above the cutoff frequency of mode 2 (see Fig. 2) and a bimodal domain with high LDOS below the cutoff frequency. Architecture 1 has lower cutoff frequency than architecture 2 by $0.0036(2\pi c/a)$. This enables a single driving field to control both architectures if they both were to be placed in a PBG circuit. For both architectures we distribute quantum dots around $\omega_A=0.285(2\pi c/a)$ with FWHM of 0.5%. In the input port of the waveguide, architecture 1 has a steady-state low intensity laser field oscillating at $0.2852(2\pi c/a)$ (slightly above central atomic transition frequency), with no output due to absorption. If we launch high intensity laser pulse in architecture 1, it will create optical pulse except with higher central frequency [see Fig. 10 (right) and Fig. 12]. This is the up-conversion switch. Both architectures 1 and 2 support identical input driving pulses and can be integrated within a single PBG optical circuit. In this tandem operation, pulses within a given circuit path can be either up-converted or down-converted and possibly amplified or simply attenuated. Up conversion followed by subsequent down conversion also enables the cascaded operation of a series of all-optical transistors whose primary input and output signal pulses are at a single frequency. Altogether, this provides the opportunity to engineer multivalued optical logic systems based on multiwavelength-channel microtransistors.

The dispersive properties (see Fig. 6) of the waveguide in architecture 3 (Fig. 5) are qualitatively different from architecture 2 and architecture 1. Architecture 3 has two bimodal frequency domains and one single-mode frequency domain in between. We center the quantum dot resonances [$\omega_A=0.3125(2\pi c/a)$] half-way between two mode cutoff frequencies and assume an inhomogeneously broadened distribution with FWHM of 0.7%. The frequency of the low intensity cw laser field in architecture 3 is chosen to be the same as the central atomic transition frequency $\omega_s=\omega_A$

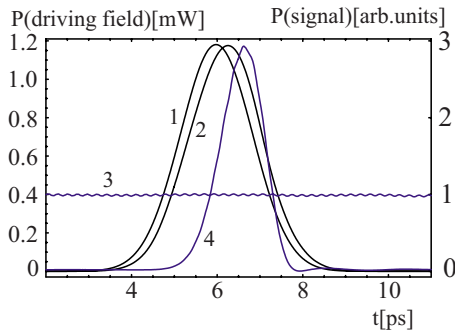


FIG. 13. (Color online) Optical frequency converter showing temporal power profile of the high intensity driving field (curves 1 and 2) and the low intensity signal field (curves 3 and 4) propagating through 20 unit cell long active part of the architecture 3 waveguide (see Fig. 5). Driving field is high intensity laser pulse, Gaussian in time with temporal duration of 2 ps and central frequency of $0.309(2\pi c/a)$. Signal field frequency is the same as the central transition frequency of quantum dots $\omega_s = \omega_A = 0.3125(2\pi c/a)$, seeded in this waveguide. Power of the driving field is rescaled to $0.3a$ thick 2D layer of one more realistic 3D heterostructure, while the low intensity signal field is measured in arbitrary units.

$= 0.3125(2\pi c/a)$. This beam is absorbed in the absence of an input driving pulse. One incoming high intensity laser pulse, with peak power of 2.36 mW, can stimulate the system to create a new output pulse with center frequency equal to the central quantum dot transition frequency (see Figs. 11, 13, and 14). But this device offers a freedom to choose one of the two driving field frequencies $\omega_d = 0.316(2\pi c/a)$ or $\omega_d = 0.309(2\pi c/a)$ in order to create the same output signal pulse. This provides the possibility of a logical OR gate if the intensity of driving pulses entering from either input wavelength channel was sufficiently large to invert the Q -dot distribution. Alternatively, if the intensity of individual driving pulses is below threshold for inversion, the simultaneously arrival of two driving pulses could invert the Q -dot distribution and architecture 3 could act as an AND gate. A more detailed picture of multiple-beam interactions with Q dots is required to describe these applications more precisely [17].

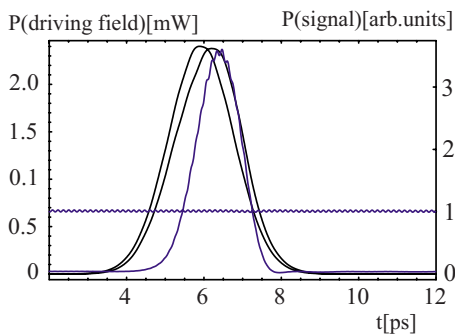


FIG. 14. (Color online) Time dependent power of the 2 ps high intensity laser pulse acting as a driving field in this optical frequency converter (curves 1 and 2) and the low intensity signal field measured at input port (curve 3) and output port (curve 4) of the 20 unit cell long nonlinear waveguide shown in Fig. 5 (architecture 3). High intensity pulse is centered at $0.316(2\pi c/a)$, while the signal field oscillates at $0.3125(2\pi c/a)$.

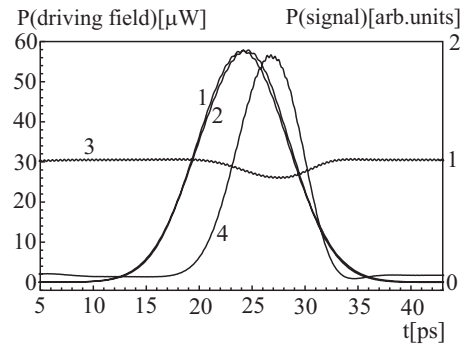


FIG. 15. Wavelength conversion of 3 nm is possible in 20 unit cell long segment of architecture 4 PC waveguide. Curves 1 and 2 define the driving field powers at the input and output ports, respectively. This pulse has Gaussian profile with temporal duration of 10 ps and peak power of $58 \mu\text{W}$. The low intensity signal field is a continuous wave (curve 3) at the input port of the waveguide, but in the output port of the waveguide signal field becomes a pulse (curve 4) with approximately Gaussian profile and temporal duration of around 7.5 ps.

The wavelength conversion described in the above examples involved moderate wavelength shifts of around 17 nm in architecture 3 and around 20 nm in architectures 1 and 2. We utilize architecture 4 to demonstrate the conditions under which a much smaller degree of wavelength conversion (3 nm) is feasible. To this end we seed the dielectric strip presented in Fig. 7 with nearly identical quantum dots (FWHM is 0.05%) at $\omega_A = 0.28795(2\pi c/a)$. Using this narrow distribution of quantum dots we achieve the required magnitude of response with a low concentration of quantum dots, $N_{\text{QD}} = 0.55 \times 10^4 \text{ dots}/(\mu\text{m})^3$. The dots are driven with one high intensity laser pulse with temporal duration of around 10 ps (suitable for application in optical telecommunication) and peak power of only $58 \mu\text{W}$, oscillating at $\omega_d = 0.28855(2\pi c/a)$. This input pulse imprints its profile onto the otherwise absorbed cw field, giving a new pulse oscillating at output signal frequency $\omega_p = 0.28791(2\pi c/a)$ (see Fig. 15), with temporal duration of 7.5 ps.

A very narrow distribution of Q dots was required in architecture 4 to separate the Q -dot resonance frequencies from the driving pulse frequency spectrum. Otherwise the driving field would simply be absorbed or amplified and device would fail. Due to the more narrow transmission spectrum of this device, it is necessary to use signal pulses with longer temporal duration. For small wavelength shifts, we use a low Q -dot density in order to limit the nonlinear response and prevent nonlinear mixing of nearby modes that make our device unstable. This limits the magnitude of the amplification possible in one short nonlinear waveguide. On the other hand, smaller wavelength shift (smaller detuning between driving and signal fields) requires smaller driving field power (compare Fig. 15 with Figs. 12–14). This illustrates a fundamental trade-off in our device. Larger wavelength shift (larger detuning between driving and signal fields) requires higher powers but allows broader Q -dot distributions. This facilitates frequency conversion of signal pulses with shorter temporal duration.

In our numerical illustrations, a very narrow quantum dot distribution was used in order to enhance the nonlinear re-

sponse to allow our device to be very compact and to operate at low power levels. The synthesis of such precise structures is a major experimental challenge. We now discuss consequences of relaxing these stringent fabrication requirements and of using larger quantum dot distributions. If architecture 1 was to be seeded with quantum dots with four times larger FWHM (2%) than described above, we would need to increase the laser field detuning from the Q -dot line center by a factor of 4 as well. Consequently, a power of around 20 mW would be required, while the temporal pulse duration could be reduced to 0.5 ps. Although a larger distribution of quantum dot frequencies provides a wider transmission spectrum, it weakens the magnitude of the transmission spectrum. In other words, the contrast between absorption and amplification becomes smaller. In order to recapture the same amplification or absorption contrast, we would need around four times as many quantum dots. This can be achieved using the same quantum dot concentration, provided that the nonlinear waveguide is made four times as long (80 unit cells).

VI. CONCLUSIONS

In summary, we have demonstrated theoretically the possibility of on-chip optical wavelength conversion in photonic band gap microcircuits using waveguide engineering and precision placement of quantum dots. Our waveguide designs require the engineering of large jump discontinuities in the local electromagnetic density of states near the transition frequencies of an inhomogeneously broadened collection of quantum dots. In our model we utilized a steady-state optical susceptibility for quantum dot resonance fluorescence in

which population switching occurs at a specific driving field intensity. A more detailed dynamical model, involving the Q -dot Bloch vector equations coupled to Maxwell's equations for pulse propagation, is needed to describe subpicosecond pulses and their wavelength conversion characteristics. In our quasi-steady-state model, we observe a fundamental balance between the magnitude of the pulse center frequency shift and width of the Q -dot inhomogeneous distribution. For a 20 nm wavelength shift a nearly 1% inhomogeneous linewidth is suitable. This provides sufficient bandwidth to process picosecond duration signal pulses. For a 3 nm wavelength shift, practically identical Q dots must be embedded in precise locations within the waveguide. The reduced operational bandwidth enables processing of pulses (without distortion) of duration 10 ps or longer. The operational power levels are also proportional to the bandwidth. Another important trade-off is between the degrees of precision in microfabrication of the overall size of the wavelength conversion device. A very precisely synthesized structure (small Q -dot inhomogeneous broadening) enables a more compact device. It is of considerable interest to extend our model to treat multiple pulses of different center frequencies arriving simultaneously to this wavelength conversion transistor. Such a generalization would enable a description of optical logic operations in a multiwavelength-channel photonic band gap circuit.

ACKNOWLEDGMENTS

This work was supported in part by the Natural Sciences and Engineering Research Council of Canada, the Canadian Institute of Advanced Research, and the Ontario Premier's Platinum Research Fund.

-
- [1] S. John, Phys. Rev. Lett. **58**, 2486 (1987).
 - [2] E. Yablonovitch, Phys. Rev. Lett. **58**, 2059 (1987).
 - [3] S. John, Phys. Rev. Lett. **53**, 2169 (1984).
 - [4] Marin Soljacic, Mihai Ibanescu, Steven G. Johnson, Yoel Fink, and J. D. Joannopoulos, Phys. Rev. E **66**, 055601(R) (2002).
 - [5] M. F. Yanik, S. Fan, M. Soljacic, and J. D. Joannopoulos, Opt. Lett. **28**, 2506 (2003).
 - [6] S. F. Mingaleev and Yu. S. Kivshar, Opt. Photonics News **13**, 48 (2002).
 - [7] D. Vujic and S. John, Phys. Rev. A **72**, 013807 (2005).
 - [8] R. Wang and S. John, Phys. Rev. A **70**, 043805 (2004).
 - [9] M. Florescu and S. John, Phys. Rev. A **69**, 053810 (2004).
 - [10] D. Vujic and S. John, Phys. Rev. A **76**, 063814 (2007).
 - [11] V. Berger, Phys. Rev. Lett. **81**, 4136 (1998).
 - [12] Xue-Hua Wang and Ben-Yuan Gu, Eur. Phys. J. B **24**, 323 (2001).
 - [13] H. Satoh, N. Yoshida, S. Kitayama, and S. Konaka, IEEE Trans. Microwave Theory Tech. **54**, 210 (2006).
 - [14] M. L. Hu, C. Y. Wang, Y. F. Li, L. Chai, and A. M. Zheltikov, Opt. Express **13**, 5947 (2005).
 - [15] Alejandro Rodriguez, Marin Soljacic, J. D. Joannopoulos, and Steven G. Johnson, Opt. Express **15**, 7303 (2007).
 - [16] A. Chutinan and S. John, Phys. Rev. E **71**, 026605 (2005).
 - [17] Xun Ma and Sajeev John (unpublished).
 - [18] K. L. Silverman, R. P. Mirin, S. T. Cundiff, and A. G. Norman, Appl. Phys. Lett. **82**, 4552 (2003).
 - [19] P. G. Eliseev, H. Li, A. Stintz, G. T. Liu, T. C. Newell, K. J. Malloy, and L. F. Lester, Appl. Phys. Lett. **77**, 262 (2000).
 - [20] U. Hohenester (unpublished).
 - [21] W. Langbein, P. Borri, U. Woggon, V. Stavarache, D. Reuter, and A. D. Wieck, Phys. Rev. B **70**, 033301 (2004).
 - [22] P. Borri, W. Langbein, S. Schneider, U. Woggon, R. L. Sellin, D. Ouyang, and D. Bimberg, Phys. Rev. Lett. **87**, 157401 (2001).
 - [23] M. Bayer and A. Forchel, Phys. Rev. B **65**, 041308(R) (2002).
 - [24] A. S. Lenihan, M. V. Gurudev Dutt, D. G. Steel, S. Ghosh, and P. K. Bhattacharya, Phys. Rev. Lett. **88**, 223601 (2002).
 - [25] S. John and T. Quang, Phys. Rev. Lett. **78**, 1888 (1997).
 - [26] A. Taflove and S. C. Hagness, *Computational Electrodynamics*, 3rd ed. (Artech House, Boston, MA, 2005).
 - [27] D. F. Kelley, IEEE Trans. Antennas Propag. **44**, 792 (1996).
 - [28] We define the laser pulse duration as a time for which power of the pulse remains above 1/2 of its maximum.
 - [29] A. Chutinan, S. John, and O. Toader, Phys. Rev. Lett. **90**, 123901 (2003).